

## Electronic Supporting Information (ESI)

### Tilt and Shift Polymorphism in Molecular Perovskites

Stefan Burger,<sup>‡a</sup> Shivani Grover,<sup>‡b</sup> Keith T. Butler,<sup>c</sup> Hanna L. B. Boström,<sup>d</sup> Ricardo Grau-Crespo<sup>\*b</sup> and Gregor Kieslich<sup>\*a</sup>

‡ shared contribution.

\* gregor.kieslich@tum.de.

\* r.grau-crespo@reading.ac.uk.

#### Contents

Experimental Procedures .....	2
Synthetic procedure for $(n\text{Pr})_3(\text{CH}_3)\text{NCl}$ .....	5
Elemental analysis for $[(\text{C}_3\text{H}_7)_3(\text{CH}_3)\text{N}]\text{M}(\text{C}_2\text{N}_3)_3$ ( $\text{M} = \text{Mn}^{2+}, \text{Co}^{2+}, \text{Ni}^{2+}$ ) .....	5
NMR data of the precursor compound $(n\text{Pr})_3(\text{CH}_3)\text{NCl}$ .....	6
Thermogravimetric analysis of $[(\text{C}_3\text{H}_7)_3(\text{CH}_3)\text{N}]\text{M}(\text{C}_2\text{N}_3)_3$ ( $\text{M} = \text{Mn}^{2+}, \text{Co}^{2+}, \text{Ni}^{2+}$ ) .....	7
Reversible Differential Scanning Calorimetry (DSC) of $[(\text{C}_3\text{H}_7)_3(\text{CH}_3)\text{N}]\text{M}(\text{C}_2\text{N}_3)_3$ ( $\text{M} = \text{Mn}^{2+}, \text{Co}^{2+}, \text{Ni}^{2+}$ ) .....	8
Fourier-transform Infrared spectroscopy (FT-IR) .....	9
Photographs of crystalline $[(\text{C}_3\text{H}_7)_3(\text{CH}_3)\text{N}]\text{M}(\text{C}_2\text{N}_3)_3$ ( $\text{M} = \text{Mn}^{2+}, \text{Co}^{2+}, \text{Ni}^{2+}$ ) .....	9
Powder X-Ray diffraction data .....	10
Single crystal X-Ray diffraction data .....	14
Quantum chemical calculations .....	19
References .....	20

## Experimental Procedures

### General information.

All chemicals used for the reactions were purchased from commercial suppliers (Sigma Aldrich, vwr) and were used without further purification. Solvents and millipore water for the syntheses and washing steps were in quality of reagent grade.

### Synthetic procedure for $(nPr)_3(CH_3)NCl$ .

The synthesis of  $C_{10}H_{24}NCl$  was carried out following a standard nucleophilic substitution reaction protocol. Tri-*n*-propylamine 1 (14.33 g, 100 mmol, 1.0 eq.) was dissolved in 70 ml acetonitrile and stirred with dropwise added methyl iodide 2 (14.19 g, 100 mmol, 1.0 eq.) in 20 ml acetonitrile at room temperature for 3 hours. After solvent removal, the residual solid was recrystallised in ethyl acetate/acetonitrile (10:1) to yield a fine, colourless powder of  $C_{10}H_{24}NI$  3. By slowly rinsing an aqueous solution of  $C_{10}H_{24}NI$  over an ion exchange resin column with subsequent elution with diluted hydrochloric acid, the iodide salt was converted into the respective chloride salt recovering  $(nPr)_3(CH_3)NCl$  4 (18.02 g, 93.0 mmol, 93.0 %) as colourless powder after evaporation of the water under reduced pressure.

### Synthesis of $[(C_3H_7)_3(CH_3)N]M(C_2N_3)_3$ ( $M = Mn^{2+}, Co^{2+}, Ni^{2+}$ ).

In a representative experiment, solutions of  $(nPr)_3(CH_3)NCl$  4 (0.2 M, 1 eq.), sodium dicyanamide  $Na(C_2N_3)$  (2.0 M, 3 eq.) and the respective metal-salt precursor ( $Mn(NO_3)_2 \cdot 4H_2O$ ,  $Co(NO_3)_2 \cdot 6H_2O$  and  $NiCl_2 \cdot 6H_2O$ , 0.2 M, 1 eq.) in ultrapure water were prepared and mixed at ambient temperature and allowed to stand for two days until large cuboid block crystals with crystal sizes between 0.5 – 1 mm were observed. The crystals were collected and washed with ice-cold ultrapure water several times, dried at room temperature and stored under air for several months with no evidence for sample degradation, *i.e.* all obtained materials are stable under ambient conditions.

For the high temperature crystallisation, precursor solutions of the three components were mixed in the same way as for the mild-solution approach, but placed in a screw-cap-sealed, pressure-tight glass vial and were heated to 95°C by means of a temperature-controlled metal block. After two days, the presence of crystalline fragments was observed, which after washing with ice-cold ultrapure water were suitable for single-crystal diffraction experiments.

### NMR data of the precursor compound $(nPr)_3(CH_3)NCl$ .

$^1H$ -NMR and  $^{13}C$ -NMR spectra were recorded on a *Bruker Avance III 400* spectrometer at room temperature. Chemical shifts are expressed as parts per million (ppm,  $\delta$ ) downfield of tetramethylsilane (TMS) and are referenced to the residual solvent signal of acetonitrile.<sup>2</sup> The description of signals include: s = singlet, t = triplet and m = multiplet. All coupling constants are absolute values and are expressed in Hertz (Hz).  $^{13}C$ -NMR was measured as  $^1H$ -NMR decoupled. All signals were assigned to the respective nuclei based on common 2D experiments like COSY, HSQC and HMBC.

### Elemental analysis for $[(C_3H_7)_3(CH_3)N]M(C_2N_3)_3$ ( $M = Mn^{2+}, Co^{2+}, Ni^{2+}$ ).

The elemental analysis experiments were carried out by the Microanalytical Laboratory of the Technical University of Munich, on an Euroanalysis instrument by *HEKAtech via* flash combustion and subsequent chromatographic separation. The elemental composition was determined twice with both measurements being in excellent agreement with the calculated values. Weighted sample amounts were between 1-2 mg.

### Thermomechanical analysis of $[(C_3H_7)_3(CH_3)N]M(C_2N_3)_3$ ( $M = Mn^{2+}, Co^{2+}, Ni^{2+}$ ).

Thermal stability of the materials was determined with a *Netzsch STA449 F5 Jupiter* machine (70  $\mu$ L aluminum oxide pans with lid). Sample amounts of 5-10 mg were heated at 10 K  $min^{-1}$  to 800°C under a constant flow of argon gas (20 mL  $min^{-1}$ ). Temperature calibration of the oven cell was performed based on the melting point of the following metals: In, Sn, Bi, Zn, Al and Au. The baseline was corrected screening an empty sample pan with the respective measurement program prior to the experiment. Thermal gravimetric analysis coupled with mass spectrometry (TG-MS) was performed on a *Netzsch STA 409* with the same temperature and heat rate program as mentioned before and evaluated mass spectrometry signal of  $H_2O$  at  $m/z$  18, while data was smoothed using a Loess filter with a span of 0.03. The onset point of thermal decomposition was calculated with the point of intersection for the two tangents of the plateau without weight loss and inflection of maximised weight loss as listed in Table S1.

Differential scanning calorimetry was conducted in a *TA Instruments DSC Q2000* with a heating rate of 10 K  $min^{-1}$  and a constant helium purging gas flow rate of 25 mL  $min^{-1}$ . The temperature window was from -150°C to 200°C and was controlled with the use of liquid nitrogen as cooling medium. The temperature of the oven cell and the heat flow signal was calibrated with respect to the melting point of indium metal and verified by the internal calibration tools provided by *TA Instruments*. The heat flow signal is shown as exo down.

### Fourier-transform Infrared spectroscopy (FT-IR)

The FTIR spectra at room temperature were collected on a *Bruker* Vertex 70 FTIR machine using a *Bruker* Platinum ATR.

### Powder X-Ray diffraction data

Measurements for bulk material analysis were performed in transmission geometry in a *STOE* STADI P (Darmstadt, Germany) diffractometer equipped with Mo  $K_{\alpha}$  radiation ( $\lambda = 0.7093 \text{ \AA}$ ), a curved Ge(111) monochromator and a *DECTRIS* Mythen 1K detector. Voltage and intensity were 50 kV and 40 mA, respectively. The measurement range was from  $2.0^{\circ}$  to  $36.0^{\circ}$  ( $2\theta$ ), with samples being fixed between two adhesive strips.

Variable temperature powder X-ray diffraction was performed in capillary mode on the same instrument using an *Oxford* Habcryo-X Cryostream 700 Cobra for temperature control with steps of 15 K. Thermal expansion coefficients are given in the section below.

All obtained Powder X-Ray diffraction patterns were analysed by performing a Pawley profile fit analysis using TOPAS Academic v6 in combination with jEdit for creating the input files.<sup>3,4</sup> Standard deviations of all parameters were calculated, and by using “randomise\_on\_errors”, it was ensured that the minimum of the refinement was reached.

### Single crystal X-Ray diffraction data

Single crystal X-Ray diffraction intensity data were collected on a *Bruker* diffractometer equipped with a TXS rotating anode with Mo- $K_{\alpha}$  radiation source ( $\lambda = 0.71073 \text{ \AA}$ ), or a *Bruker* “D8 Venture Duo IMS” diffractometer equipped with an IMS microsource anode for fine-focus with a Mo- $K_{\alpha}$  radiation source, a CMOS plate detector (*Bruker* APEX III,  $\kappa$ -CMOS) and Helios optics, or on a *Bruker* “D8 Kappa Apex II” with a fine-focus sealed tube and a *Triumph* monochromator. For temperature control, an *Oxford* Cryosystems cooling device was used. Machine control was enabled by using the APEX2 (D8 Kappa) or the APEX3 (TXS, IMS) software package.<sup>5</sup> Appropriate crystals were selected under a microscope in perfluorinated ether, fixed on top of a kapton micro sampler (*MiTeGen*), transferred to the diffractometer and frozen under a stream of cold nitrogen. A matrix scan was used to determine the initial lattice parameters. Reflections were merged and corrected for Lorentz and polarisation effects, scan speed, and background using SAINT.<sup>6</sup> Absorption corrections, including odd and even ordered spherical harmonics were performed using SADABS.<sup>7</sup> Space group assignments were based upon systematic absences, E-statistics, and successful refinement of the structures. Data reduction was performed with APEX3 and structure solution was performed by using SHELX as integrated in Olex2.<sup>8–10</sup> Structures were solved by direct methods with the aid of successive difference Fourier maps, and were refined against all data. Hydrogen atoms were placed in calculated positions and refined using a riding model. Non-hydrogen atoms were refined with anisotropic displacement parameters. Full-matrix least-squares refinements were carried out by minimising  $\sum_w(F_o^2 - F_c^2)^2$  with the SHELXL weighting scheme.<sup>8</sup> The visualisation of the crystal structures were generated using VESTA 3.4.0.<sup>11</sup>

### Quantum chemical calculations

**Density functional theory simulations.** Our calculations are based on the density functional theory (DFT) as implemented in the Vienna Ab Initio Simulation Package (VASP).<sup>12,13</sup> The exchange-correlation energy of electrons is treated within the generalised gradient approximation (GGA) with the functional by Perdew, Burke and Ernzerhof (PBE).<sup>14</sup> In order to account for the limitations of the GGA to describe the d-orbitals of transition metals, we included Hubbard corrections for these orbitals (GGA+U), following the formalism introduced by Dudarev et al.,<sup>15</sup> where a single parameter ( $U_{\text{eff}}$ ) controls the strength of the correction. The  $U_{\text{eff}}$  parameters for Mn (4.0 eV), Co (3.3 eV), and Ni (6.4 eV) were taken from the work by Wang et al.,<sup>16</sup> where they were fitted so that GGA+U could reproduce the experimental oxidation energies in transition metal oxides. We also included dispersion corrections following Grimme’s D3 scheme.<sup>17</sup> The projector augmented wave (PAW) method<sup>18,19</sup> was used to describe the interactions between the valence electrons and the frozen cores, which consisted of orbitals up to 1s for C and N, and up to 3p for the transition metals. We used an energy cut-off of 520 eV to truncate the planewave expansion of the Kohn-Sham wavefunctions, which was 30% above the default cut-off for the employed PAW potentials, to minimise Pulay errors. Brillouin zone (BZ) integrations were performed by sampling the reciprocal space using  $\Gamma$ -centred meshes of  $4 \times 3 \times 2$  k-points with reference to orthorhombic unit cell and of  $4 \times 4 \times 4$  k-points with reference to rhombohedral unit cell, which give similarly dense grids. Spin polarisation was allowed in all calculations to properly describe the magnetic transition metal cations.

**Phonon simulations.** Given the large size of the crystallographic unit cells, phonon dispersion curves were obtained from forces constants calculated by systematic displacements of ionic positions only within the unit cell, *via* the Phonopy code.<sup>20</sup> Representative phonon dispersion curves (in the case of the Mn compounds) for the orthorhombic and rhombohedral cells are shown in Fig. S13 a) and b). We are showing only the low-frequency region, but the phonon spectrum extends up to  $3200 \text{ cm}^{-1}$ .

The use of a single unit cell in the simulations, together with the softness of the low-frequency modes, led to numerical noise which translated into artificial imaginary modes in the phonon dispersion curves, away from the Brillouin centre. These imaginary frequencies could not be resolved by following the imaginary modes with ionic displacement in larger supercells (using the ModeMap code by Skelton et al.).<sup>21</sup> For example, the potential energy surfaces obtained by displacing the ions in the direction of eigenvectors for lowest-frequency bands at the F point for the rhombohedral phase, or for the U point for the orthorhombic phase, using appropriate supercells, showed normal convexity with a minimum at the optimised structures for both phases, Fig. S13 c). We therefore conclude that both structures are dynamically stable, representing local minima of the potential energy surface.

**Synthetic procedure for  $(nPr)_3(CH_3)NCl$ .**

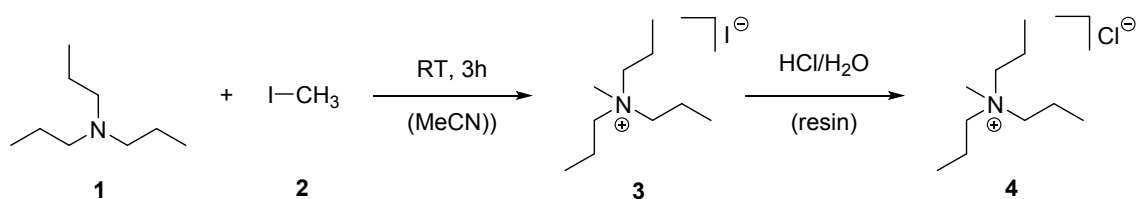


Fig. S1 Schematic of the synthesis route for  $(nPr)_3(CH_3)NCl$  following the Menshutkin reaction type.<sup>1</sup>

**Elemental analysis for  $[(C_3H_7)_3(CH_3)N]M(C_2N_3)_3$  ( $M = Mn^{2+}, Co^{2+}, Ni^{2+}$ ).**

Elemental analysis calcd (%) for  $[(C_3H_7)_3(CH_3)N]Mn(C_2N_3)_3$ : C 46.72 H 5.88 N 34.05 Mn 13.35; found1 C 46.75 H 5.88 N 33.96, found2 C 46.85 H 5.90 N 34.06.

Elemental analysis calcd (%) for  $[(C_3H_7)_3(CH_3)N]Co(C_2N_3)_3$ : C 46.27 H 5.82 N 33.72 Co 14.19; found1 C 46.31 H 5.77 N 33.58, found2 C 46.35 H 5.80 N 33.64.

Elemental analysis calcd (%) for  $[(C_3H_7)_3(CH_3)N]Ni(C_2N_3)_3$ : C 46.29 H 5.83 N 33.74 Ni 14.14; found1 C 46.47 H 5.86 N 33.79, found2 C 46.58 H 5.87 N 33.87.

NMR data of the precursor compound  $(nPr)_3(CH_3)NCl$ .

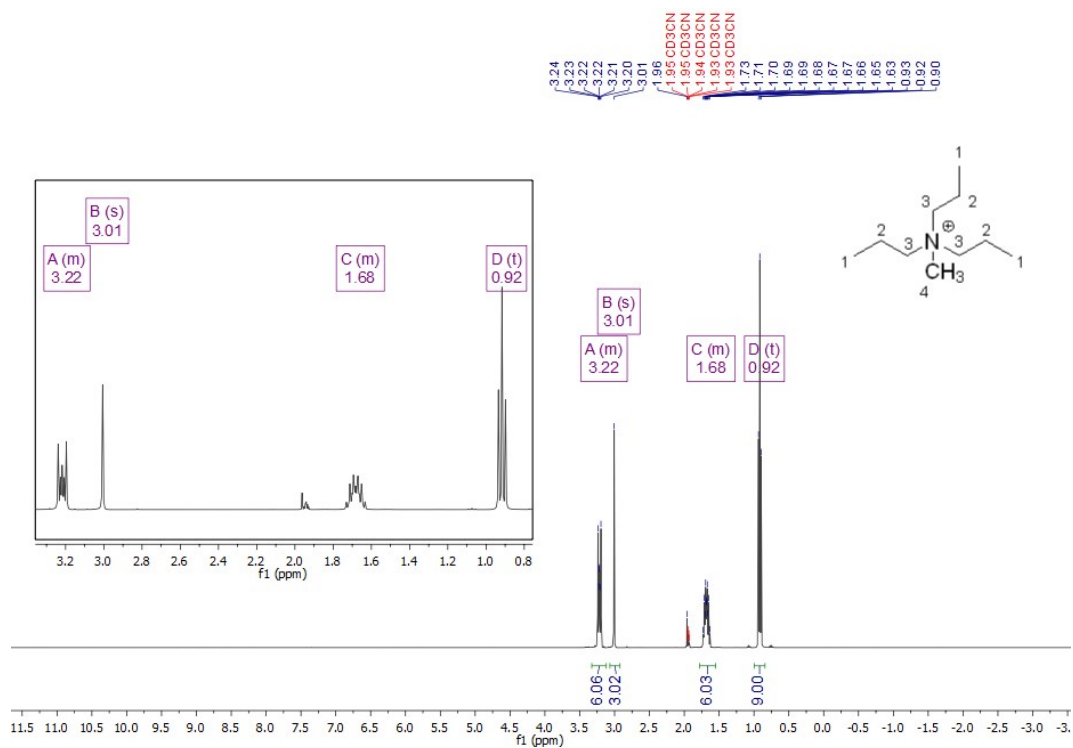


Fig. S2  $^1H$ -NMR spectrum of  $(nPr)_3(CH_3)NCl$  in acetonitrile- $d_3$ .

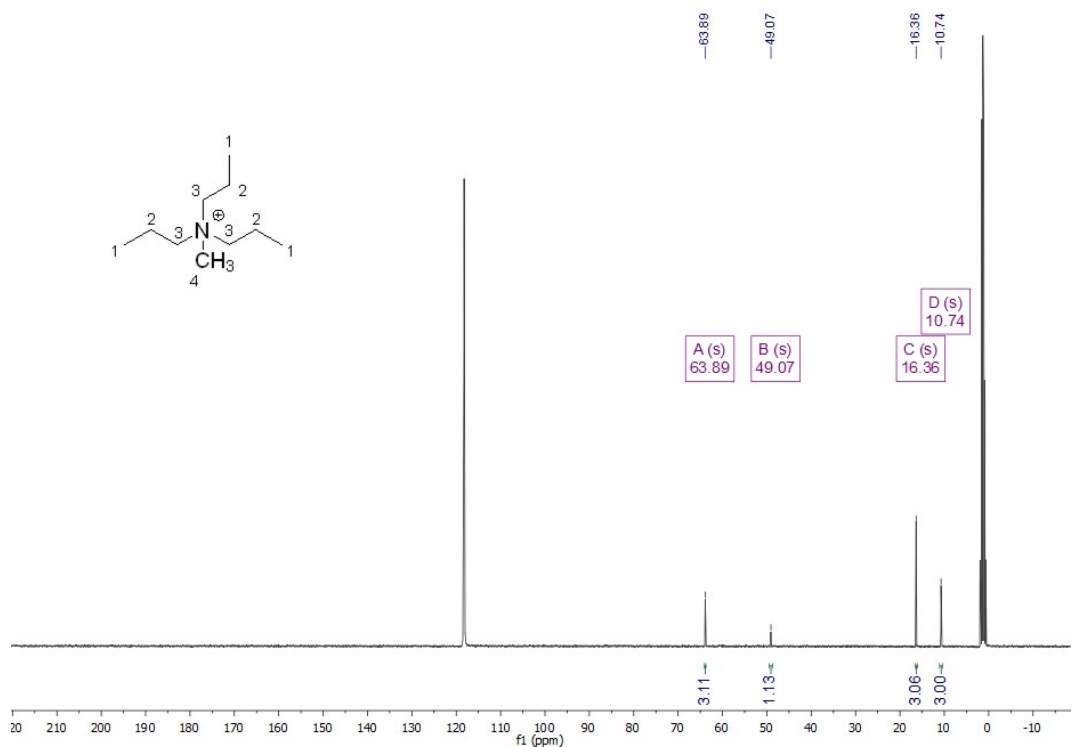


Fig. S3  $^{13}C$ -NMR spectrum of  $(nPr)_3(CH_3)NCl$  in acetonitrile- $d_3$  with residual NMR solvent signals at  $\delta$  [ppm] = 118.26 (s) and 1.32 (hept).

$^1H$ -NMR (400 MHz, Acetonitrile- $d_3$ , 298 K):  $\delta$  [ppm] = 3.28 – 3.16 (m, 6H, C3-H), 3.01 (s, 3H, C4-H), 1.76 – 1.60 (m, 6H, C2-H), 0.92 (t,  $J$  = 7.3 Hz, 9H, C1-H).

$^{13}C$ -NMR (101 MHz, Acetonitrile- $d_3$ , 298 K):  $\delta$  [ppm] = 63.89 (C3), 49.07 (C4), 16.36 (C2), 10.74 (C1).

Thermogravimetric analysis of  $[(C_3H_7)_3(CH_3)N]M(C_2N_3)_3$  ( $M = Mn^{2+}, Co^{2+}, Ni^{2+}$ ).

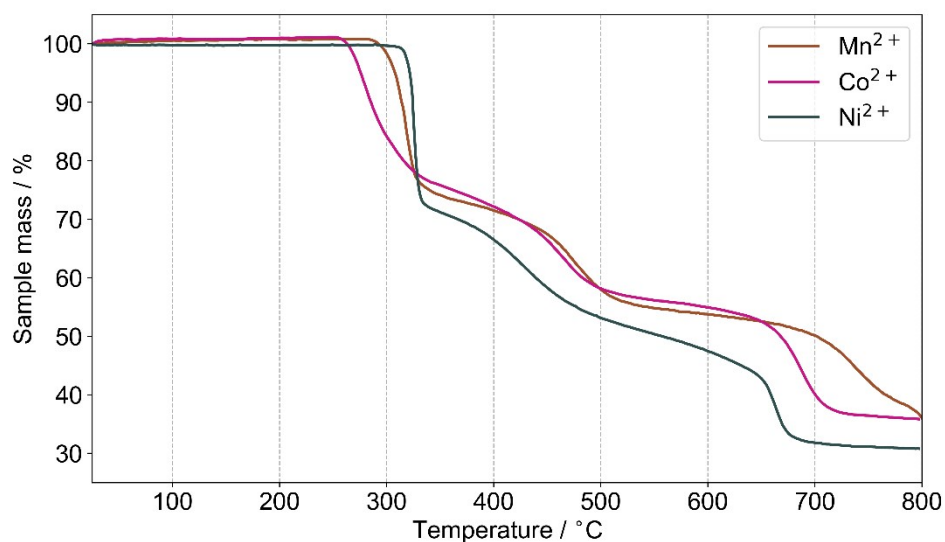


Fig. S4 TGA curves of  $[(C_3H_7)_3(CH_3)N]M(C_2N_3)_3$  with  $M$  being  $Mn^{2+}$  (brown),  $Co^{2+}$  (violet) and  $Ni^{2+}$  (dark green), indicating the thermal stability in an argon atmosphere.

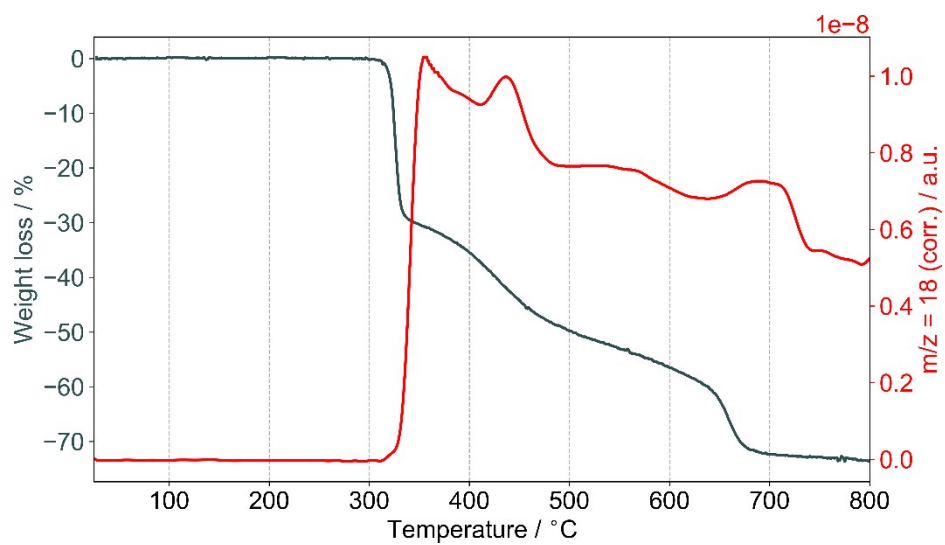


Fig. S5 Additional TGA curve (grey) coupled with mass spectrometry (red) for  $[(C_3H_7)_3(CH_3)N]Ni(C_2N_3)_3$ , showing no signs of weight loss during heating until the decomposition temperature.

Reversible Differential Scanning Calorimetry (DSC) of  $[(C_3H_7)_3(CH_3)N]M(C_2N_3)_3$  ( $M = Mn^{2+}, Co^{2+}, Ni^{2+}$ ).

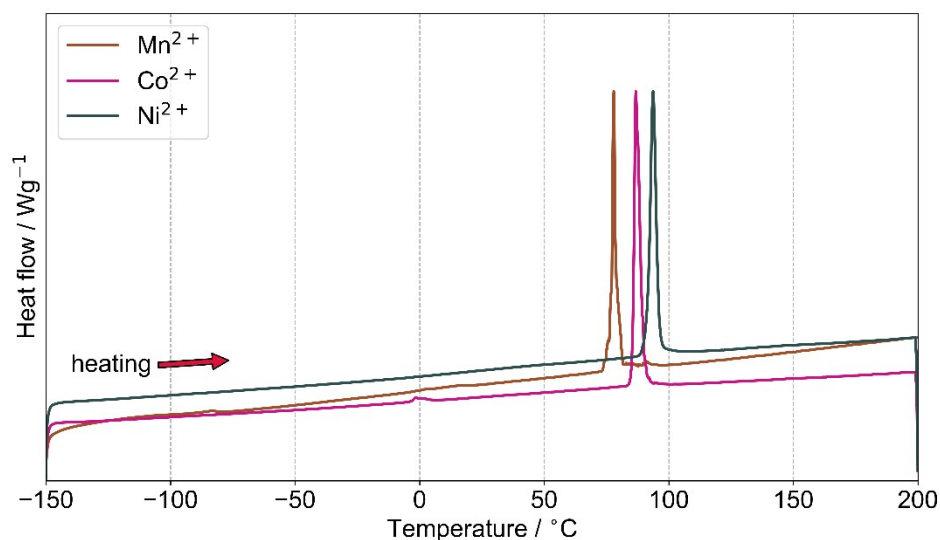


Fig. S6 Differential scanning calorimetry measurement for  $[(nPr)_3(CH_3)N]M(C_2N_3)_3$ . Shown is the curve for the first heating step of the as-synthesised materials from  $-150^\circ\text{C}$  to  $200^\circ\text{C}$ , highlighting the irreversible phase transition from the ambient  $Pnma$  phase to the high temperature  $R\bar{3}c$  phase. Colour code: brown -  $Mn^{2+}$ , violet -  $Co^{2+}$ , dark green -  $Ni^{2+}$ . Results including temperature of the phase transitions are summarised in Table S1.

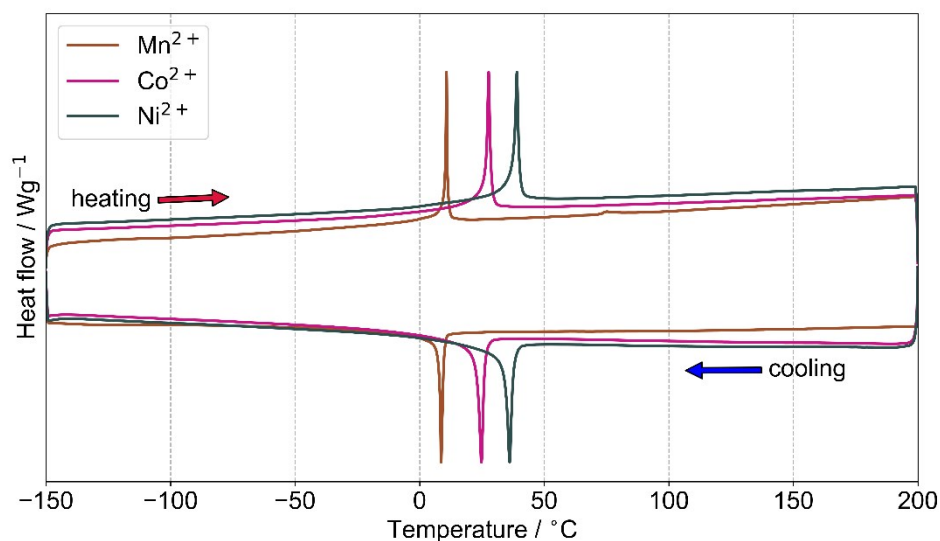


Fig. S7 Reversible differential scanning calorimetry measurement for  $[(nPr)_3(CH_3)N]M(C_2N_3)_3$ . Shown is the cyclic curve for the cooling with subsequent re-heating step of the materials after initial heat treatment, see Figure S6. Illustrated is the reversible rhombohedral-to-rhombohedral phase transition which is accessed when the as-synthesised samples are heated. Colour code: brown -  $Mn^{2+}$ , violet -  $Co^{2+}$ , dark green -  $Ni^{2+}$ . Thermodynamic characteristics for the phase transitions are summarised in Table S1.

Tab. S1 Phase transition characteristics for  $[(C_3H_7)_3(CH_3)N]M(C_2N_3)_3$  extracted from differential scanning calorimetry data with temperatures and enthalpies for the irreversible phase transition (Figure S6) as well as the reversible transition (Figure S7). Additionally, the decomposition temperature observed by TGA is listed.

M =	$T(\text{decomp.})^{[a]}$	$T_{PT}(\text{irrev.})^{[a]}$	$\Delta H_{PT}(\text{irrev.})^{[b]}$	$T_{PT}(\text{rev.})^{[a]}$	$\Delta H_{PT}(\text{rev.})^{[b]}$	$\Delta S_{PT}(\text{rev.})^{[c]}$
$Mn^{2+}$	304.8	76.9	7507.5	10.8	4932.3	17.4
$Co^{2+}$	263.6	85.4	8074.6	27.7	5324.9	17.7
$Ni^{2+}$	323.9	91.6	6629.5	39.0	5616.6	18.0

[a] in  $^\circ\text{C}$ . [b] in  $\text{J mol}^{-1}$ . [c] in  $\text{J (K mol)}^{-1}$ .



## Fourier-transform Infrared spectroscopy (FT-IR)

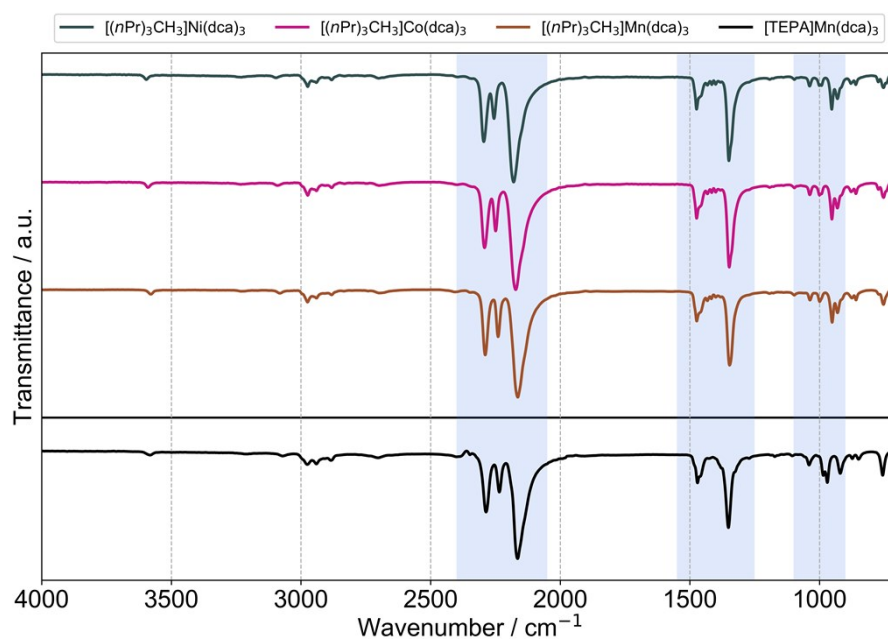


**Fig. S8** FT-IR spectra at room temperature for the as-synthesised series of  $[(C_3H_7)_3(CH_3)N]M(C_2N_3)_3$  with  $M$  being  $Mn^{2+}$  (brown),  $Co^{2+}$  (violet) and  $Ni^{2+}$  (dark green), indicating the isostructural nature of the three compounds. Additionally, the reference IR spectrum for  $[(C_3H_7)_4N]Mn(C_2N_3)_3$  (black) is shown, which shows the same signal arrangement as the  $[(C_3H_7)_3(CH_3)N]M(C_2N_3)_3$  series, typical for 3D dicyanamide-based molecular perovskites with  $\nu^- = 2300-2100\text{ cm}^{-1}$  (dca vibration modes),  $1500-1300\text{ cm}^{-1}$  ( $CH_x$  vibration modes) and  $1050-950\text{ cm}^{-1}$  (C-C and C-N-C vibrations). For a detailed assignment of all vibration modes to the respective signals/wavenumbers we would like to refer to ref. [23] where the authors assigned experimental IR modes for  $[(C_3H_7)_4N]Cd(C_2N_3)_3$ .

## Photographs of crystalline $[(C_3H_7)_3(CH_3)N]M(C_2N_3)_3$ ( $M = Mn^{2+}, Co^{2+}, Ni^{2+}$ ).



**Fig. S9** Batch photographs of crystalline material  $[(C_3H_7)_3(CH_3)N]M(C_2N_3)_3$  as synthesised in sample vials, with  $M$  being  $Mn^{2+}$  (left),  $Co^{2+}$  (middle) and  $Ni^{2+}$  (right). Crystallite sizes vary from 100 – 1000  $\mu\text{m}$ .

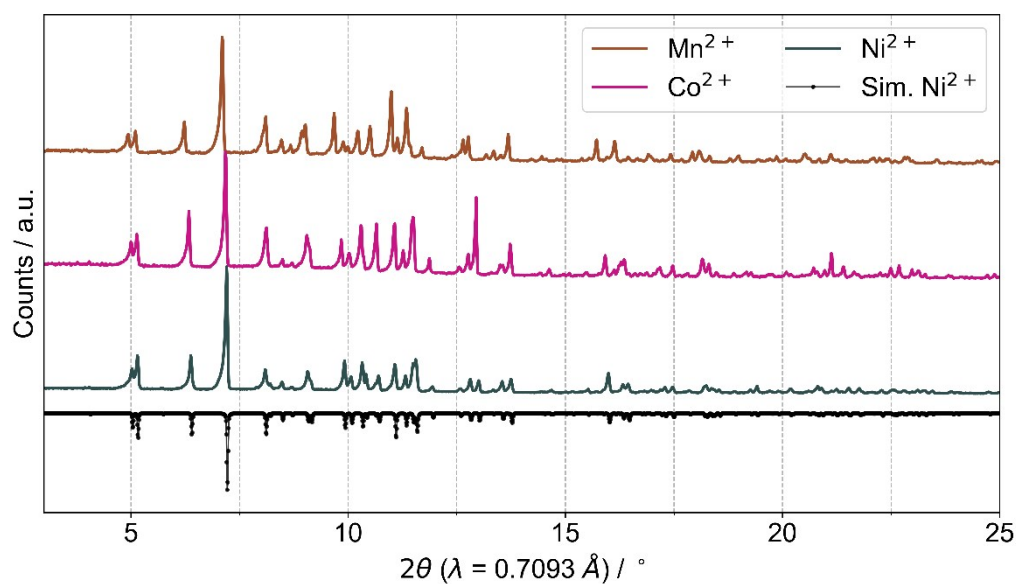


**Fig. S10** Powder X-ray diffraction patterns of the as-synthesised bulk materials of  $[(n\text{Pr})_3(\text{CH}_3)\text{N}]\text{M}(\text{C}_2\text{N}_3)_3$  based on an in-house ( $\lambda = 0.7093 \text{ \AA}$ ) molybdenum source device at room temperature. Shown in black at the bottom is the simulated powder pattern from crystal structure obtained *via* single crystal X-ray diffraction at room temperature for the  $\text{Ni}^{2+}$  containing compound, with the observed powder patterns for  $[(n\text{Pr})_3(\text{CH}_3)\text{N}]\text{M}(\text{C}_2\text{N}_3)_3$  with  $M$  being  $\text{Ni}^{2+}$  in dark green,  $\text{Co}^{2+}$  in violet and  $\text{Mn}^{2+}$  in brown, confirming the bulk phase purity and isostructural phase of the three samples.

#### Powder X-Ray diffraction data

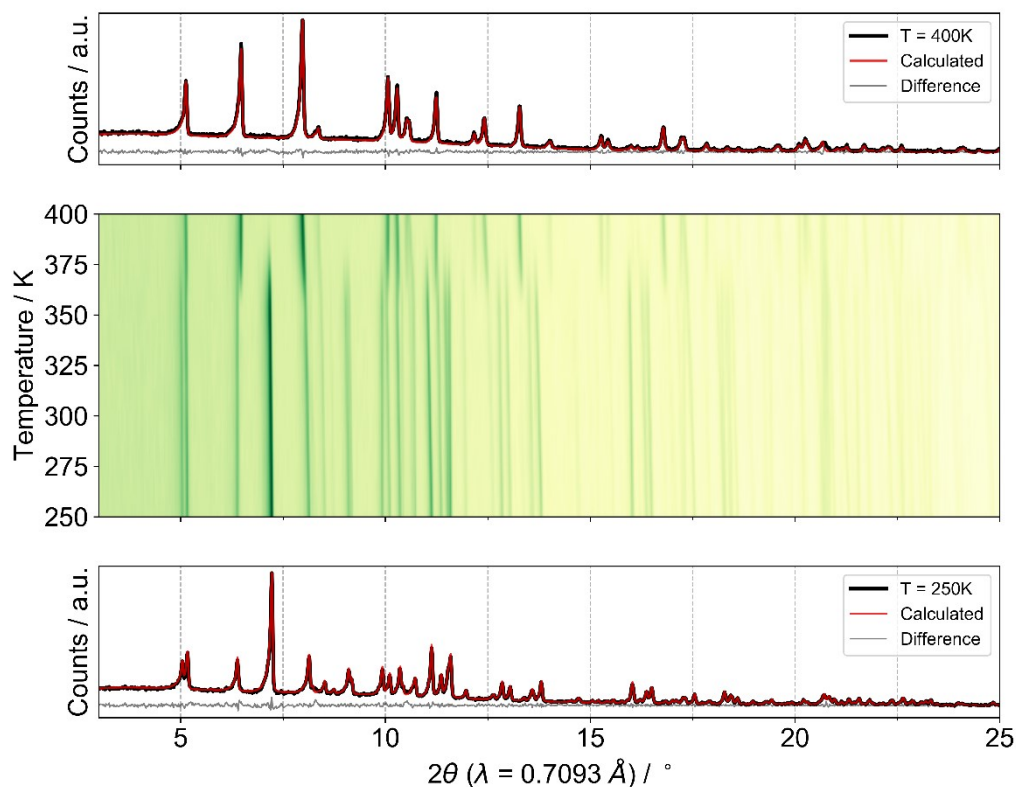


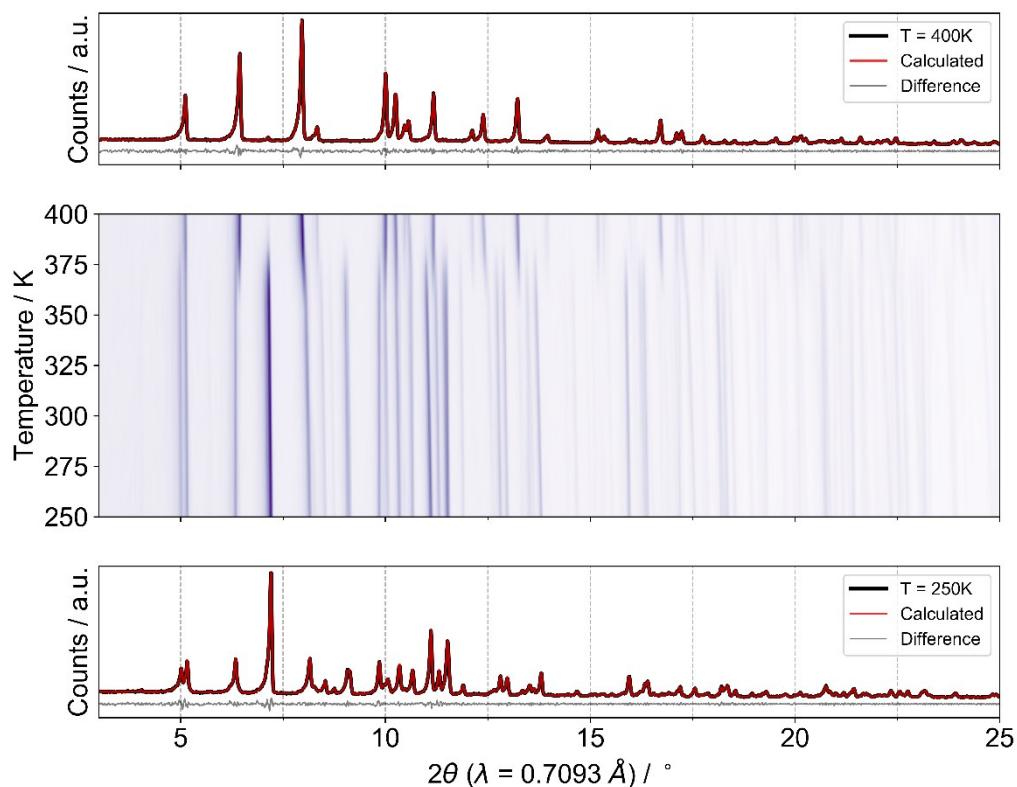
**Fig. S11** Variable-temperature powder XRD patterns of  $[(n\text{Pr})_3(\text{CH}_3)\text{N}]\text{Ni}(\text{C}_2\text{N}_3)_3$  for the as-prepared orthorhombic phase. The bottom panel shows the Pawley profile fit outcome of the pattern at 250 K, serving as the starting point for sequenced analysis of the respective temperature points till 400 K for which the profile fit is shown on top of the plot. In the middle of the plot are the experimental data of variable temperature experiments illustrated as heat map with deeper colour corresponding to a higher intensity in the respective Bragg reflection.

**Tab. S2** Refined cell parameters and deviations for  $[(n\text{Pr})_3(\text{CH}_3)\text{N}]\text{Ni}(\text{C}_2\text{N}_3)_3$  at temperatures from 250 K to 400 K, using the Pawley profile fit analysis method. Additionally, the output of PASCAL - principal axis strain calculations<sup>22</sup> with direction of projections of the three principal axes on the unit cell axes  $a$ ,  $b$  and  $c$  is shown. Listed are the resulting thermal expansion coefficients  $\alpha$  as well as the direction of propagation of the thermal response.

$T / \text{K}$	$r_{\text{wp}}$	$a / \text{\AA}$	$b / \text{\AA}$	$c / \text{\AA}$	$V / \text{\AA}^3$
250	4.1533	9.9842(6)	16.0860(10)	12.7032(9)	2040.2(2)
265	3.9511	9.9960(6)	16.0977(9)	12.7047(7)	2044.3(2)
280	3.8460	10.0108(6)	16.1134(9)	12.7033(7)	2049.2(2)
295	3.8132	10.0254(5)	16.1256(8)	12.7050(7)	2054.0(2)
310	3.6465	10.0400(5)	16.1410(8)	12.7036(7)	2058.7(2)
325	3.8173	10.0539(5)	16.1541(8)	12.7059(6)	2063.6(2)
340	3.6567	10.0707(4)	16.1696(7)	12.7050(6)	2068.9(2)
355	3.8018	10.0884(5)	16.1852(8)	12.7048(6)	2074.5(2)
370	3.2951	10.1044(16)	16.2011(21)	12.7063(12)	2080.0(5)

Axes	$\alpha / (\text{MK})^{-1}$	$\sigma\alpha / (\text{MK})^{-1}$	$a$	$b$	$c$
$X_1$	0.8203	0.5042	0.0000	0.0000	1.0000
$X_2$	59.3014	1.0540	0.0000	1.0000	0.0000
$X_3$	100.4661	2.0829	-1.0000	0.0000	0.0000
$V$	161.7253	3.5036			



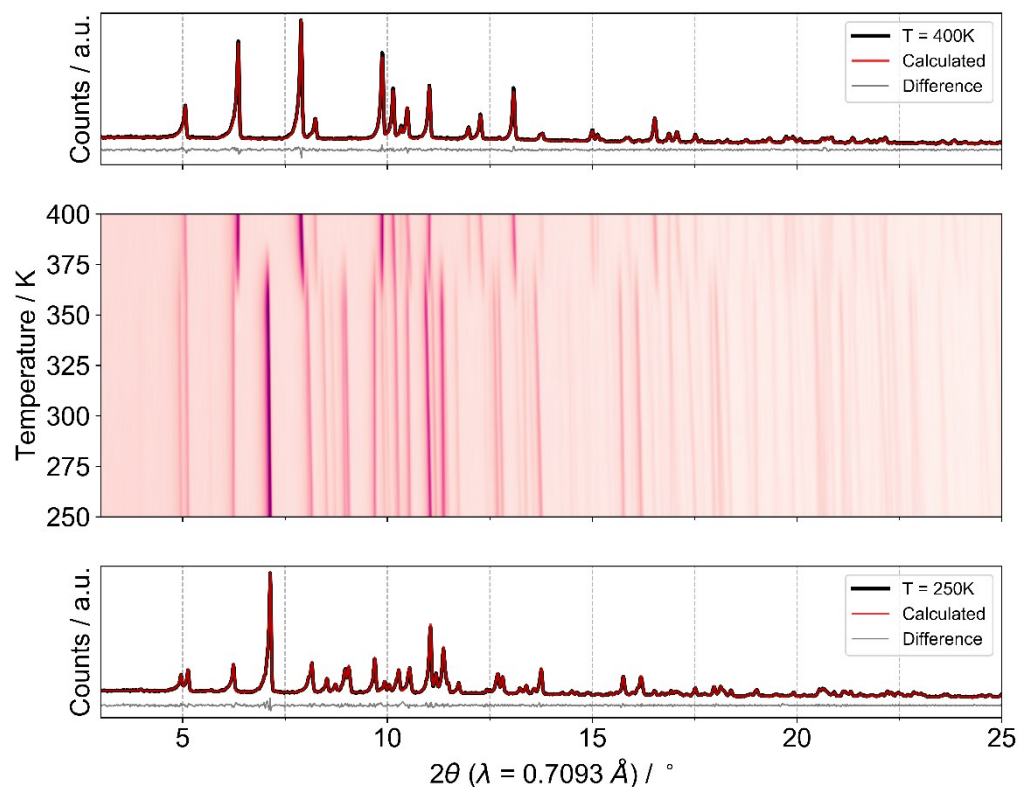
**Fig. S12** Variable-temperature powder XRD patterns of  $[(n\text{Pr})_3(\text{CH}_3)\text{N}]\text{Co}(\text{C}_2\text{N}_3)_3$  for the as-prepared orthorhombic phase. The bottom panel shows the Pawley profile fit outcome of the pattern at 250 K, serving as the starting point for sequenced analysis of the respective temperature points till 400 K for which the profile fit is shown on top of the plot. In the middle of the plot are the experimental data of variable temperature experiments illustrated as heat map with deeper colour corresponding to a higher intensity in the respective Bragg reflection.

**Tab. S3** Refined cell parameters and deviations for  $[(n\text{Pr})_3(\text{CH}_3)\text{N}]\text{Co}(\text{C}_2\text{N}_3)_3$  at temperatures from 250 K to 400 K, using the Pawley profile fit analysis method. Additionally, the output of PASCAL - principal axis strain calculations with direction of projections of the three principal axes on the unit cell axes  $a$ ,  $b$  and  $c$  is shown. Listed are the resulting thermal expansion coefficients  $\alpha$  as well as the direction of propagation of the thermal response.

$T / \text{K}$	$r_{\text{wp}}$	$a / \text{\AA}$	$b / \text{\AA}$	$c / \text{\AA}$	$V / \text{\AA}^3$
250	3.2877	9.9721(4)	16.1778(7)	12.8061(6)	2066.0(1)
265	3.3928	9.9865(3)	16.1919(5)	12.8066(5)	2070.8(1)
280	3.5148	10.0011(3)	16.2055(6)	12.8065(5)	2075.6(1)
295	3.3842	10.0159(3)	16.2212(6)	12.8067(5)	2080.7(1)
310	3.4712	10.0306(4)	16.2353(5)	12.8075(5)	2085.7(1)
325	3.2966	10.0474(4)	16.2499(5)	12.8063(5)	2090.9(1)
340	3.4113	10.0626(4)	16.2659(6)	12.8072(5)	2096.2(1)
355	3.3138	10.0805(4)	16.2809(6)	12.8063(4)	2101.8(1)
370	3.1826	10.0998(6)	16.2956(9)	12.8052(6)	2107.5(2)

Axes	$\alpha / (\text{MK})^{-1}$	$\sigma\alpha / (\text{MK})^{-1}$	$a$	$b$	$c$
$X_1$	-0.4676	0.3846	0.0000	0.0000	1.0000
$X_2$	60.6959	0.4817	0.0000	1.0000	0.0000
$X_3$	105.4286	2.0554	-1.0000	0.0000	0.0000
$V$	166.5718	2.1850			



**Fig. S13** Variable-temperature powder XRD patterns of  $[(n\text{Pr})_3(\text{CH}_3)\text{N}]\text{Mn}(\text{C}_2\text{N}_3)_3$  for the as-prepared orthorhombic phase. The bottom panel shows the Pawley profile fit outcome of the pattern at 250 K, serving as the starting point for sequenced analysis of the respective temperature points till 400 K for which the profile fit is shown on top of the plot. In the middle of the plot are the experimental data of variable temperature experiments illustrated as heat map with deeper colour corresponding to a higher intensity in the respective Bragg reflection.

**Tab. S4** Refined cell parameters and deviations for  $[(n\text{Pr})_3(\text{CH}_3)\text{N}]\text{M}(\text{C}_2\text{N}_3)_3$  at temperatures from 250 K to 400 K, using the Pawley profile fit analysis method. Additionally, the output of PASCAL - principal axis strain calculations with direction of projections of the three principal axes on the unit cell axes  $a$ ,  $b$  and  $c$  is shown. Listed are the resulting thermal expansion coefficients  $\alpha$  as well as the direction of propagation of the thermal response.

$T / \text{K}$	$r_{\text{wp}}$	$a / \text{\AA}$	$b / \text{\AA}$	$c / \text{\AA}$	$V / \text{\AA}^3$
250	3.4619	9.9727(3)	16.3817(6)	13.0213(4)	2127.3(1)
265	3.5507	9.9877(3)	16.3962(6)	13.0226(4)	2132.6(1)
280	3.1339	10.0046(3)	16.4135(5)	13.0237(4)	2138.6(1)
295	3.2508	10.0210(3)	16.4294(5)	13.0232(4)	2144.1(1)
310	3.1952	10.0387(3)	16.4474(5)	13.0246(4)	2150.5(1)
325	3.3884	10.0543(3)	16.4633(6)	13.0255(5)	2156.1(1)
340	3.4424	10.0732(3)	16.4816(6)	13.0275(5)	2162.9(1)
355	3.5132	10.0921(3)	16.4984(6)	13.0270(5)	2169.1(1)

Axes	$\alpha / (\text{MK})^{-1}$	$\sigma\alpha / (\text{MK})^{-1}$	$a$	$b$	$c$
$X_1$	-4.4959	2.2322	0.0000	0.0000	1.0000
$X_2$	69.6802	0.7471	0.0000	1.0000	0.0000
$X_3$	107.4559	0.9771	-1.0000	0.0000	0.0000
$V$	174.3908	2.4237			

**Tab. S5** Summary of cell and refinement parameters for the material series  $[(n\text{Pr})_3(\text{CH}_3)\text{N}]\text{M}(\text{C}_2\text{N}_3)_3$  at 250 K for the as-synthesised polymorph P(M)-I and for the transformed polymorph P(M)-IIb at 400 K which served as starting and end point for the sequential analysis of the variable temperature powder diffraction experiments.

$M$	$a / \text{\AA}$	$b / \text{\AA}$	$c / \text{\AA}$	$\alpha, \beta, \gamma / ^\circ$	$r_{\text{wp}}$	$r_{\text{exp}}$	GOF
250 K, space group $Pnma$							
$\text{Mn}^{2+}$	9.9747(3)	16.3853(7)	13.0237(5)	90, 90, 90	3.4116	3.4606	0.986
$\text{Co}^{2+}$	9.9721(4)	16.1778(7)	12.8061(6)	90, 90, 90	3.2877	3.1628	1.039
$\text{Ni}^{2+}$	9.9842(6)	16.0860(10)	12.7032(9)	90, 90, 90	4.1533	3.8669	1.074

$M$	$a / \text{\AA}$	$c / \text{\AA}$	$\alpha, \beta, \gamma / ^\circ$	$r_{\text{wp}}$	$r_{\text{exp}}$	GOF
400 K, space group $R\bar{3}c$						
$\text{Mn}^{2+}$	12.7867(2)	23.2773(5)	90, 90, 120	3.7574	4.0794	0.921
$\text{Co}^{2+}$	12.6107(2)	23.0957(7)	90, 90, 120	3.0832	3.1515	0.978
$\text{Ni}^{2+}$	12.5288(3)	23.0607(9)	90, 90, 120	4.6015	4.5611	1.009

Comment to the thermal expansion behaviour of  $[(n\text{Pr})_3(\text{CH}_3)\text{N}]\text{M}(\text{C}_2\text{N}_3)_3$ :

We observe an anisotropic thermal expansion behaviour for the as-synthesised phase P(M)-I with no or little uniaxial negative thermal expansion in  $X_1$  direction and strong positive thermal expansion in  $X_3$  direction. The anisotropic behaviour increases from  $\text{Ni}^{2+}$  to  $\text{Mn}^{2+}$ . This leads to an overall positive thermal volume expansion, which lies in the range of magnitude of the related molecular perovskite series  $[(\text{C}_3\text{H}_7)_4\text{N}]\text{M}(\text{C}_2\text{N}_3)_3$ .<sup>23</sup>

## Single crystal X-Ray diffraction data

**Tab. S6** Summary of crystallographic data of  $[(nPr)_3(CH_3)N]M(C_2N_3)_3$  for the as-synthesised orthorhombic P(M)-I phases.

Compound	$[(nPr)_3CH_3]Ni(C_2N_3)_3$	$[(nPr)_3CH_3]Ni(C_2N_3)_3$	$[(nPr)_3CH_3]Co(C_2N_3)_3$	$[(nPr)_3CH_3]Mn(C_2N_3)_3$
Empirical formula	$C_{16}H_{24}N_{10}Ni$	$C_{16}H_{24}N_{10}Ni$	$C_{16}H_{24}N_{10}Co$	$C_{16}H_{24}N_{10}Mn$
Formula weight / $(g\text{mol})^{-1}$	415.16	415.16	415.38	411.39
Temperature / K	100.0	300.0	298.0	298.0
Crystal system	orthorhombic	orthorhombic	orthorhombic	orthorhombic
Space group	<i>Pnma</i>	<i>Pnma</i>	<i>Pnma</i>	<i>Pnma</i>
<i>a</i> / Å	9.8624(6)	10.0232(3)	10.0138(2)	10.0193(5)
<i>b</i> / Å	15.9509(9)	16.1193(5)	16.2151(4)	16.4215(10)
<i>c</i> / Å	12.6923(7)	12.6992(4)	12.7967(3)	13.0125(7)
$\alpha$ / °	90	90	90	90
$\beta$ / °	90	90	90	90
$\gamma$ / °	90	90	90	90
Volume / Å <sup>3</sup>	1996.7(2)	2051.77(11)	2077.86(8)	2141.0(2)
Z	4	4	4	4
$\rho_{\text{calc}}$ / $g\text{cm}^{-3}$	1.381	1.344	1.328	1.276
$\mu$ / $\text{mm}^{-1}$	0.995	0.968	0.848	0.638
F (000)	872.0	872.0	868.0	860.0
Crystal size / $\text{mm}^{-3}$	$0.307 \times 0.202 \times 0.169$	$0.261 \times 0.219 \times 0.179$	$0.384 \times 0.305 \times 0.226$	$0.285 \times 0.278 \times 0.27$
Radiation	$\text{MoK}\alpha$ ( $\lambda = 0.71073$ )	$\text{MoK}\alpha$ ( $\lambda = 0.71073$ )	$\text{MoK}\alpha$ ( $\lambda = 0.71073$ )	$\text{MoK}\alpha$ ( $\lambda = 0.71073$ )
2 $\theta$ range for data collection / °	4.102 to 59.146	5.054 to 57.398	4.054 to 52.736	3.994 to 52.742
Index ranges	$-13 \leq h \leq 13$ $-22 \leq k \leq 22$ $-17 \leq l \leq 17$	$-13 \leq h \leq 13$ $-21 \leq k \leq 21$ $-16 \leq l \leq 17$	$-12 \leq h \leq 12$ $-20 \leq k \leq 20$ $-15 \leq l \leq 15$	$-12 \leq h \leq 12$ $-20 \leq k \leq 20$ $-16 \leq l \leq 16$
Reflections collected	116055	77417	100185	28206
Independent reflections	2893 $R_{\text{int}} = 0.0482$ $R_{\text{sigma}} = 0.0141$	2734 $R_{\text{int}} = 0.0379$ $R_{\text{sigma}} = 0.0094$	2206 $R_{\text{int}} = 0.0250$ $R_{\text{sigma}} = 0.0079$	2271 $R_{\text{int}} = 0.0374$ $R_{\text{sigma}} = 0.0183$
Data/restraints/parameters	2893/0/189	2734/0/177	2206/0/183	2271/0/170
Goodness of fit on $F^2$	1.197	1.051	1.071	1.020
Final R indexes [ $I > 2\sigma(I)$ ]	$R_1 = 0.0385$ $wR_2 = 0.0985$	$R_1 = 0.0283$ $wR_2 = 0.0738$	$R_1 = 0.0252$ $wR_2 = 0.0758$	$R_1 = 0.0294$ $wR_2 = 0.0779$
Final R indexes [all data]	$R_1 = 0.0427$ $wR_2 = 0.1008$	$R_1 = 0.0390$ $wR_2 = 0.0805$	$R_1 = 0.0270$ $wR_2 = 0.0780$	$R_1 = 0.0462$ $wR_2 = 0.0888$
Largest diff. peak/hole / $e\text{Å}^{-3}$	0.43/−0.46	0.28/−0.34	0.25/−0.33	0.21/−0.26
Flack parameter <sup>24</sup>	---	---	---	---
CCDC number	2068712	2068716	2068842	2068843

**Tab. S7** Summary of crystallographic data of [(nPr)<sub>3</sub>(CH<sub>3</sub>)N]M(C<sub>2</sub>N<sub>3</sub>)<sub>3</sub> for the rhombohedral P(M)-IIa phases.

Compound	[(nPr) <sub>3</sub> CH <sub>3</sub> ]Ni(C <sub>2</sub> N <sub>3</sub> ) <sub>3</sub>	[(nPr) <sub>3</sub> CH <sub>3</sub> ]Co(C <sub>2</sub> N <sub>3</sub> ) <sub>3</sub>	[(nPr) <sub>3</sub> CH <sub>3</sub> ]Mn(C <sub>2</sub> N <sub>3</sub> ) <sub>3</sub>
Empirical formula	C <sub>16</sub> H <sub>24</sub> N <sub>10</sub> Ni	C <sub>16</sub> H <sub>24</sub> N <sub>10</sub> Co	C <sub>16</sub> H <sub>24</sub> N <sub>10</sub> Mn
Formula weight / (g mol) <sup>-1</sup>	415.16	415.38	411.39
Temperature / K	100.0	100.0	100.0
Crystal system	trigonal	trigonal	trigonal
Space group	<i>R</i> 3 <i>c</i>	<i>R</i> 3 <i>c</i>	<i>R</i> 3 <i>c</i>
<i>a</i> / Å	12.5883(8)	12.6783(16)	12.8301(13)
<i>b</i> / Å	12.5883(8)	12.6783(16)	12.8301(13)
<i>c</i> / Å	21.565(2)	21.585(5)	21.750(3)
$\alpha$ / °	90	90	90
$\beta$ / °	90	90	90
$\gamma$ / °	120	120	120
Volume / Å <sup>3</sup>	2959.5(5)	3004.7(10)	3100.7(8)
Z	6	6	6
$\rho_{\text{calc}}$ / g cm <sup>-3</sup>	1.398	1.377	1.322
$\mu$ / mm <sup>-1</sup>	1.007	0.880	0.661
F (000)	1308.0	1302.0	1290.0
Crystal size / mm <sup>-3</sup>	0.314 × 0.277 × 0.16	0.246 × 0.204 × 0.18	0.176 × 0.122 × 0.107
Radiation	MoK $\alpha$ ( $\lambda$ = 0.71073)	MoK $\alpha$ ( $\lambda$ = 0.71073)	MoK $\alpha$ ( $\lambda$ = 0.71073)
2 $\theta$ range for data collection / °	5.314 to 59.15	5.292 to 56.554	5.242 to 55.728
Index ranges	-16 ≤ <i>h</i> ≤ 17 -16 ≤ <i>k</i> ≤ 17 -29 ≤ <i>l</i> ≤ 29	-16 ≤ <i>h</i> ≤ 15 -16 ≤ <i>k</i> ≤ 16 -28 ≤ <i>l</i> ≤ 26	-16 ≤ <i>h</i> ≤ 16 -16 ≤ <i>k</i> ≤ 16 -28 ≤ <i>l</i> ≤ 28
Reflections collected	16219	15254	14822
Independent reflections	1840	1650	1650
	$R_{\text{int}} = 0.0266$	$R_{\text{int}} = 0.0252$	$R_{\text{int}} = 0.0675$
	$R_{\text{sigma}} = 0.0165$	$R_{\text{sigma}} = 0.0148$	$R_{\text{sigma}} = 0.0377$
Data/restraints/parameters	1840/1/87	1650/1/87	1650/1/87
Goodness of fit on F <sup>2</sup>	1.047	1.090	1.082
Final R indexes [ <i>I</i> > 2 $\sigma$ ( <i>I</i> )]	$R_1 = 0.0161$ $wR_2 = 0.0401$	$R_1 = 0.0166$ $wR_2 = 0.0410$	$R_1 = 0.0396$ $wR_2 = 0.0983$
Final R indexes [all data]	$R_1 = 0.0173$ $wR_2 = 0.0408$	$R_1 = 0.0183$ $wR_2 = 0.0429$	$R_1 = 0.0480$ $wR_2 = 0.1039$
Largest diff. peak/hole / eÅ <sup>-3</sup>	0.20/-0.24	0.17/-0.17	0.86/-0.46
Flack parameter <sup>24</sup>	0.443(15)	0.448(19)	0.36(5)
Flack parameter_s.u.	0.015	0.019	0.050
CCDC number	2068844	2068846	2068848

**Tab. S8** Summary of crystallographic data of  $[(n\text{Pr})_3(\text{CH}_3)\text{N}]\text{M}(\text{C}_2\text{N}_3)_3$  for the rhombohedral P(M)-IIb phases.

Compound	$[(n\text{Pr})_3\text{CH}_3]\text{Ni}(\text{C}_2\text{N}_3)_3$	$[(n\text{Pr})_3\text{CH}_3]\text{Co}(\text{C}_2\text{N}_3)_3$	$[(n\text{Pr})_3\text{CH}_3]\text{Mn}(\text{C}_2\text{N}_3)_3$
Empirical formula	$\text{C}_{16}\text{H}_{24}\text{N}_{10}\text{Ni}$	$\text{C}_{16}\text{H}_{24}\text{N}_{10}\text{Co}$	$\text{C}_{16}\text{H}_{24}\text{N}_{10}\text{Mn}$
Formula weight / (g mol) <sup>-1</sup>	415.16	415.38	411.39
Temperature / K	350.0	350.0	350.0
Crystal system	trigonal	trigonal	trigonal
Space group	$\overline{R}3c$	$\overline{R}3c$	$\overline{R}3c$
$a / \text{\AA}$	12.5350(3)	12.6131(2)	12.7694(5)
$b / \text{\AA}$	12.5350(3)	12.6131(2)	12.7694(5)
$c / \text{\AA}$	22.8074(12)	22.8639(6)	23.0222(13)
$\alpha / ^\circ$	90	90	90
$\beta / ^\circ$	90	90	90
$\gamma / ^\circ$	120	120	120
Volume / $\text{\AA}^3$	3103.5(2)	3150.10(13)	3251.0(3)
Z	6	6	6
$\rho_{\text{calc}} / \text{g cm}^{-3}$	1.333	1.314	1.261
$\mu / \text{mm}^{-1}$	0.960	0.839	0.630
F (000)	1308.0	1302.0	1290.0
Crystal size / mm <sup>-3</sup>	0.314 × 0.277 × 0.16	0.218 × 0.157 × 0.142	0.185 × 0.169 × 0.12
Radiation	MoK $\alpha$ ( $\lambda = 0.71073$ )	MoK $\alpha$ ( $\lambda = 0.71073$ )	MoK $\alpha$ ( $\lambda = 0.71073$ )
2 $\theta$ range for data collection / $^\circ$	5.18 to 55.736	5.158 to 57.378	5.108 to 59.12
Index ranges	-16 ≤ h ≤ 15 -16 ≤ k ≤ 16 -29 ≤ l ≤ 30	-16 ≤ h ≤ 15 -17 ≤ k ≤ 16 -30 ≤ l ≤ 30	-17 ≤ h ≤ 17 -17 ≤ k ≤ 17 -31 ≤ l ≤ 31
Reflections collected	17980	17146	57844
Independent reflections	830	907	1025
	$R_{\text{int}} = 0.0199$	$R_{\text{int}} = 0.0219$	$R_{\text{int}} = 0.0359$
Data/restraints/parameters	830/84/103	907/60/94	1025/63/94
Goodness of fit on $F^2$	1.107	1.133	1.095
Final R indexes [ $I > 2\sigma(I)$ ]	$R_1 = 0.0234$ $wR_2 = 0.0656$	$R_1 = 0.0249$ $wR_2 = 0.0691$	$R_1 = 0.0391$ $wR_2 = 0.1197$
Final R indexes [all data]	$R_1 = 0.0261$ $wR_2 = 0.0691$	$R_1 = 0.0312$ $wR_2 = 0.0749$	$R_1 = 0.0513$ $wR_2 = 0.1317$
Largest diff. peak/hole / e $\text{\AA}^{-3}$	0.16/-0.47	0.13/-0.22	0.16/-0.29
Flack parameter <sup>24</sup>	---	---	---
CCDC number	2068845	2068847	2068849



**Tab. S9** Torsion angles for the two polymorphs **P-(Ni)-I** and **P(Ni)-IIa** at 100 K. The torsion angle belongs to the metal atom and the respective dicyanamide molecule as bent linker. The two terminal and the central N atoms of dicyanamide are used to determine the angle. This defines the torsion angles as follows:  $\alpha(1) = \text{Ni}(1)\text{-N}(1)\text{-N}(3)\text{-N}(5)$  and  $\alpha(2) = \text{N}(1)\text{-N}(3)\text{-N}(5)\text{-Ni}(2)$  and results in the respective binding mode geometry with  $\alpha < 90^\circ$  representing **syn** geometry and  $\alpha > 90^\circ$  being **anti** geometry. Additionally, the crystallographic directions are given in analogy to Figure 2 of the manuscript.

Direction	Atom number	Torsion angle / °	Binding mode
<b>P(Ni)-I, orthorhombic <i>Pnma</i></b>			
[010]	Ni1-N3-N5-N3	99.2(8)	<b>anti</b>
	N3-N5-N3-Ni1	99.2(8)	<b>anti</b>
[101]	Ni1-N4-N6-N7	108.3(3)	anti
	N4-N6-N7-Ni1	87.8(3)	syn
[10 $\bar{1}$ ]	Ni1-N7-N6-N4	87.8(3)	syn
	N7-N6-N4-Ni1	108.3(3)	anti
<b>P(Ni)-IIa, rhombohedral <i>R3c</i></b>			
[1 $\bar{1}$ 0]	Ni1-N2-N5-N3	117.67(18)	anti
	N2-N5-N3-Ni1	86.6(8)	syn
[011]	Ni1-N3-N5-N2	86.6(8)	syn
	N3-N5-N2-Ni1	117.67(18)	anti
[10 $\bar{1}$ ]	Ni1-N3-N5-N2	86.6(8)	syn
	N3-N5-N2-Ni1	117.67(18)	anti

Statement on the absolute structure determination of the polymorph phases P(M)-IIa; here exemplarily based on the Ni-compound, however, this applies to the isostructural Co- and Mn- analogues in the same manner as they show the same checkCIF comment:

Output of the (IUCr) checkCIF procedure for  $[(n\text{Pr})_3\text{CH}_3]\text{Ni}(\text{C}_2\text{N}_3)_3$ :

STRVA01\_ALERT\_4\_C: Flack test results are ambiguous.

From the CIF: `_refine_ls_abs_structure_Flack` 0.443.

From the CIF: `_refine_ls_abs_structure_Flack_su` 0.015.

PURPOSE: To check that `_refine_ls_abs_structure_flack` is within expected limits.

*"The correct absolute structure has been defined by the atomic coordinates if `_refine_ls_abs_structure_flack` is close to 0.0 (and the s.u. is sufficiently small).*

*In cases of intermediate values of `_refine_ls_abs_structure_flack`, a merohedral twin or a partial mix of enantiomers may be present and this fact should be discussed in the manuscript. However, intermediate values might also be obtained when the absolute structure parameter is essentially meaningless because the compound is a weak anomalous scatterer."*

It is known for rhombohedral symmetry and non-centrosymmetric space groups that (merohedral) twinning of single crystals is prone to occur which may be solved using the twin law (0 1 0 1 0 0 0 -1).<sup>25</sup> Treatment of the diffraction data with this law delivers the same structural model. However, since this twin matrix corresponds to the inverted symmetry operation of the non-centrosymmetric Laue group of the crystal structure, the presented diffraction data are treated with the inversion operator which is a common method for absolute structure determination with Flack parameters.<sup>24</sup>

Since the `ls_abs_structure_Flack_s.u.` values for all three compounds with  $\text{Ni}^{2+}$ ,  $\text{Co}^{2+}$  and  $\text{Mn}^{2+}$  are close to 0.0 after refinement and the Flack parameters are close to  $x = 0.5$  (which would mean racemic or twinned), we believe our structure determination treating the data as inversion twin gives a reliable model for the absolute crystal structure.

E-statistics  $|E^2-1|$  for the rhombohedral structural models (0.736: non-centrosymmetric; 0.968: centrosymmetric):

$[(n\text{Pr})_3\text{CH}_3]\text{Mn}(\text{C}_2\text{N}_3)_3$ : 0.795 (100 K), 0.990 (350 K)

$[(n\text{Pr})_3\text{CH}_3]\text{Co}(\text{C}_2\text{N}_3)_3$ : 0.843 (100 K), 0.974 (350 K)

$[(n\text{Pr})_3\text{CH}_3]\text{Ni}(\text{C}_2\text{N}_3)_3$ : 0.826 (100 K), 0.943 (350 K)

To confirm the ordered structure in polar  $R\bar{3}c$ , we tried to refine the low-temperature data in the centrosymmetric space group  $R\bar{3}c$ . However, as we were not able to refine a reliable structural model in  $R\bar{3}c$  for the ordered structures, we state the structural model in the polar, non-centrosymmetric space group  $R\bar{3}c$  being appropriate, in addition to the information given by the E-statistics which confirms our assumption.

## Quantum chemical calculations

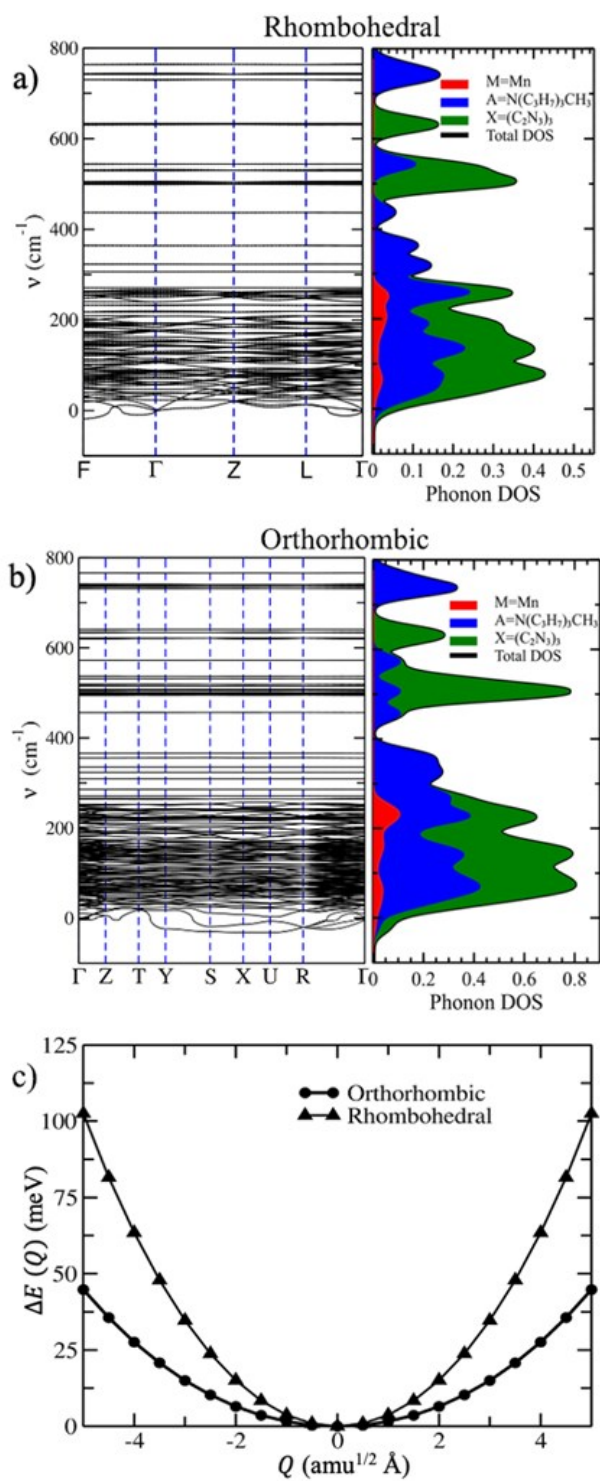


**Fig. S14** Phonon dispersion curves and partial density of states in the low-frequency region for the Mn-containing materials in a) the rhombohedral and b) the orthorhombic phase, calculated using a unit cell; c) Potential energy surfaces in the direction of eigenvectors for lowest-frequency bands at the F point for the rhombohedral phase, and U point for the orthorhombic phase, using appropriate supercells.

## References

- 1 N. Menshutkin, *Z. Phys. Chem.*, 1890, **5U**.
- 2 G. R. Fulmer, A. J. M. Miller, N. H. Sherden, H. E. Gottlieb, A. Nudelman, B. M. Stoltz, J. E. Bercaw and K. I. Goldberg, *Organometallics*, 2010, **29**, 2176.
- 3 G. S. Pawley, *J. Appl. Cryst.*, 1981, **14**, 357.
- 4 A. A. Coelho, *J. Appl. Cryst.*, 2018, **51**, 210.
- 5 APEX3 suite of crystallographic software, *Bruker AXS Inc. Madison Wisconsin USA*, **2015**, Version 5.2.
- 6 SAINT, *Bruker AXS Inc., Madison, Wisconsin, USA*, **2014**, Version 8.34A.
- 7 SADABS, *Bruker AXS Inc., Madison, Wisconsin, USA*, **2014**, Version 2014/5.
- 8 G. M. Sheldrick, *Acta Crystallogr. Sect. C*, 2015, **71**, 3.
- 9 G. M. Sheldrick, *Acta Crystallogr. Sect. A*, 2015, **71**, 3.
- 10 O. V. Dolomanov, L. J. Bourhis, R. J. Gildea, J. A. K. Howard and H. Puschmann, *J. Appl. Crystallogr.*, 2009, **42**, 339.
- 11 K. Momma and F. Izumi, *J. Appl. Cryst.*, 2011, **44**, 1272.
- 12 G. Kresse and J. Furthmüller, *Comput. Mater. Sci.*, 1996, **6**, 15.
- 13 Kresse and Furthmüller, *Phys. Rev. B Condens. Matter*, 1996, **54**, 11169.
- 14 Perdew, Burke and Ernzerhof, *Proc. Natl. Acad. Sci. USA*, 1996, **77**, 3865.
- 15 S. L. Dudarev, G. A. Botton, S. Y. Savrasov, C. J. Humphreys and A. P. Sutton, *Phys. Rev. B Condens. Matter*, 1998, **57**, 1505.
- 16 L. Wang, T. Maxisch and G. Ceder, *Phys. Rev. B*, 2006, **73**, 603.
- 17 S. Grimme, J. Antony, S. Ehrlich and H. Krieg, *J. Chem. Phys.*, 2010, **132**, 154104.
- 18 Blöchl, *Phys. Rev. B Condens. Matter*, 1994, **50**, 17953.
- 19 G. Kresse and D. Joubert, *Phys. Rev. B Condens. Matter*, 1999, **59**, 1758.
- 20 A. Togo and I. Tanaka, *Scr. Mater.*, 2015, **108**, 1.
- 21 J. M. Skelton, L. A. Burton, S. C. Parker, A. Walsh, C.-E. Kim, A. Soon, J. Buckeridge, A. A. Sokol, C. R. A. Catlow, A. Togo and I. Tanaka, *Phys. Rev. Lett.*, 2016, **117**, 75502.
- 22 M. J. Cliffe and A. L. Goodwin, *J. Appl. Cryst.*, 2012, **45**, 1321.
- 23 J. M. Bermúdez-García, M. Sánchez-Andújar, S. Yáñez-Vilar, S. Castro-García, R. Artiaga, J. López-Beceiro, L. Botana, Á. Alegria and M. A. Señarís-Rodríguez, *Inorg. Chem.*, 2015, **54**, 11680.
- 24 H. D. Flack, *Acta Cryst. A*, 1983, **39**, 876.
- 25 S. Parsons, *Acta Cryst. D*, 2003, **59**, 1995.